Copper nanoclusters: Selective CO_2 to methane conversion beyond 1 A/cm^2

Mahdi Salehi [a], Hasan Al-Mahayni [a], Amirhossein Farzi [a], Morgan McKee [c,d], Sepideh Kaviani [b], Elmira Pajootan [a], Roger Lin [a], Nikolay Kornienko [c,d], Ali Seifitokaldani [a,*]

[a] Department of Chemical Engineering, McGill University, Montréal, Quebec, Canada
[b] Department of Chemistry, McGill University, Montréal, Quebec, Canada
[c] Department of Chemistry, Université de Montréal, Montréal, Quebec, Canada
[d] Institute of Inorganic Chemistry, University of Bonn, Gerhard-Domagk-Str. 1, Bonn 53121, Germany

A B S T R A C T

Carbon dioxide offers a unique opportunity as a feedstock for energy production through electrocatalysis. Methane production holds promise for its widespread applications and market demand. However, commercial viability faces challenges of low selectivity, current density, and high applied potential. Efforts to improve methane selectivity while suppressing multi-carbon products, e.g., ethylene, often involve lower alkalinity electrolytes. However, it reduces current density due to increased ohmic resistance without significant gains in the reaction yield. This study utilizes quantum mechanics computations to design a nano-cluster copper catalyst that redirects the reaction pathway from ethylene towards methane, even under alkaline conditions. We achieved a Faradaic efficiency (FE) of 85 %, a current density of 1.5 A/cm^2, and stability of over 10 hours solely by controlling particle size in copper catalysts. This work paves the way to overcoming current limitations in electrocatalytic methane production and holds broader implications for advancing sustainable CO_2 utilization in energy systems.

1. Introduction

Alleviating the greenhouse gas (GHG) emission and CO_2 concentration in the atmosphere is a universal research priority to curb the global warming [1–3]. Electrochemical CO_2 reduction reaction (CO_2RR) is a promising route to convert CO_2 into value-added chemical feedstocks and fuels by converting renewable yet intermittent electricity such as wind-, hydro-, and solar-electricity into storable chemical energy. This approach not only minimizes CO_2 emissions by closing the carbon loop, but also generates reliable chemical and energy sources [4–7]. Among different CO_2RR products, methane is particularly desirable. As the primary component of natural gas, methane is widely employed for electricity and heat generation due to its substantial energy capacity [8, 9]. In addition, infrastructures for its storage, distribution, and utilization are already well-established [10–15]. Nevertheless, the economic viability of methane production through the CO_2RR remains a challenge, primarily due to its low cost when derived from fossil fuels. This underscores the need for the development of a sustainable, long-term pathway for methane production.

Previous studies on CO_2RR have employed various strategies to

enhance methane selectivity, such as adjusting CO_2 partial pressure [14–16], utilizing low-coordinated Cu clusters [17,18], incorporating metal/metal oxide doping with Cu [2,11], and employing single-atom catalysts [8,19–21]. Copper-supported iron-single-atom catalyst, for instance, produced methane at a Faradaic efficiency (FE) of 64 % and a current density of 200 mA/cm^2 [8]. In another study, Cu^{2+} ions were incorporated into a CeO_2 matrix to strengthen the *CO adsorption (* denotes the catalyst surface), facilitating its hydrogenation into CH_4 rather than the formation of multi-carbon (C_{2+}) intermediates. This catalyst obtained a FE of 67.8 % for methane at a current density of 200 mA/cm^2, while the ethylene FE was as low as 3.6 % [22]. Using less alkaline electrolytes, Cu-Al catalyst doped with uniformly dispersed Ga with a low *CO binding energy, achieved a methane FE of 53 % and suppressed the hydrogen evolution reaction (HER) to 23 % at −1.4 V vs. RHE (reversible hydrogen electrode) [11]. It is also shown that incorporating Au into Cu under limiting *CO adsorption conditions, such as low CO_2 concentrations, promotes *CO protonation over C-C coupling and weakens surface *H adsorption, ultimately enhancing methane selectivity. An optimized composition of Au-Cu catalyst, and under controlled CO_2 concentration, a methane FE of 56 % and a current

* Corresponding author.
E-mail address: ali.seifitokaldani@mcgill.ca (A. Seifitokaldani).

density of 112 mA/cm^2 was obtained [12]. While these strategies have enhanced methane production, they have not significantly improved selectivity, current density, or lowered the relatively high applied potential. Consequently, the cost of methane production exceeds $6000 per tonne, which is substantially higher than alternative methods like thermochemical ($2797 per tonne) and biochemical ($2830 per tonne) approaches, not even factoring in methane derived from conventional and unconventional shale gas sources [23]. To reduce production costs and make CO$_2$RR technology viable for industrial applications, we must enhance the catalyst's electrical selectivity for methane by increasing Faradaic efficiency and reaction rates [23].

The CO$_2$ mass diffusion limitations in conventional H-cell setups (Fig. S1A) were effectively overcome by utilizing a flow cell design (Fig. S1B), resulting in an increased current density. [24–26]. Furthermore, in flow cells, the gas diffusion electrode (GDE) separates CO$_2$ gas from the electrolyte. This allows the use of highly alkaline solutions with greater ionic conductivity as a model system [27–30], and reducing both ohmic resistance and voltage loss [24,31]. However, using alkaline electrolytes like potassium hydroxide (KOH) promotes C-C coupling, leading to increased multi-carbon product (C$_{2+}$) formation like ethylene [31]. Consequently, this reduces both current density and FE for methane. For the same reason, in most reported studies, less alkaline electrolytes such as potassium bicarbonate (KHCO$_3$) are used to achieve a high FE towards methane, albeit at a low current density and a high overpotential [19,32–36].

Literature has also extensively focused on catalyst engineering to improve selectivity. Controlling the crystallinity of copper catalysts has proven effective in switching the reaction pathway between ethylene and methane production [7,37–42]. In the field of electrocatalysis, it's widely accepted that Cu(100) is favorable for C-C coupling and ethylene formation, while Cu(111) surfaces make C$_1$ products like methane more likely. Density functional theory (DFT) calculations revealed that facet-dependent selectivity is due to varying adsorption energies of CH$_4$ and C$_2$H$_4$ intermediates on different Cu facets [38,43]. The effect of the size of the catalyst on the selectivity is also investigated for Cu nano-octahedra catalysts [44]. Experiments with various sizes of Cu nano-octahedra demonstrated that smaller Cu particles (75 nm) exhibit higher selectivity for CH$_4$ production, achieving a 55 % FE for CH$_4$ at -1.25 V vs. RHE and a total current density of 1.5 mA/cm^2, in contrast to larger particles with sizes of 150 and 310 nm. In this study, it is speculated that catalytic sites at the interface between two facets promote CO$_2$RR over HER, potentially by stabilizing key intermediates like *CO and *COOH. While an in-depth analysis of the underlying reaction mechanism is lacking, this approach presents a promising path to catalyst size engineering for enhanced selectivity towards desired products. The use of low coordinated copper catalysts in a membrane electrode assembly (MEA) was also proposed as a novel strategy for methane production [17]. Computational studies suggested that undercoordinated copper promotes methane production, a finding corroborated by experimental results, which achieved a 62 % methane FE and a partial current density of 136 mA/cm^2 even under highly alkaline conditions [17]. However, the effect of the shape and facets of the nanoparticles, still need to be investigated to distinguish the effects of size, crystallinity, and coordination environment on catalytic performance. In another work, Zhang et al., showed the introduction of an asymmetric low-frequency pulsed strategy (ALPS) has significantly improved the selectivity and stability of copper-based catalysts, notably the Cu-dimethylpyrazole complex Cu$_3$(DMPz)$_3$, for CO$_2$RR towards methane production. This method not only enhances methane selectivity (achieving Faradaic efficiencies over 76.6 % for 24 hours and maintaining stability for up to 300 hours) but also modulates the copper oxidation states to optimize the catalytic process [45].

The present study, on the other hand, investigates the relationship between the size of a particle and its crystallinity, and aims to understand its impact on the CO$_2$RR selectivity. Our DFT computations encompass both large crystalline surfaces, commonly used in literature via periodic slab models, and extremely small nanoparticles using isolated nano-cluster models. We systematically investigate the CO$_2$RR mechanism on these catalysts. By calculating the excess energy, we established a relationship between particle size and the most stable crystalline structure at sizes below 1 nm. We observed that smaller particle sizes expose more Cu(111) facets on the surface, while as the particle size increases, the ratio of Cu(100) to Cu(111) facets rises rapidly. Consequently, stable large particles (>2 nm) form polycrystals with multiple facets, including Cu(111), Cu(100), and Cu(110). Furthermore, we found that small particles with Cu(111) as the dominant facet not only promote the methane pathway but also, surprisingly, strongly adsorb any produced ethylene on the nanocluster, which leads to the uncoupling of the C-C bond and the subsequent generation of methane. This observation suggests that even alkaline electrolytes that facilitate multi-carbon product formation are likely to result in methane formation. Guided by these DFT computations, we synthesized Cu nanoparticles with nominal sizes ranging from 0.5 nm to 200 nm. We observed a clear shift in selectivity from ethylene to methane as particle size decreased. Notably, we achieved methane production in highly alkaline electrolytes (e.g., 1 M KOH) with an exceptional FE of 85 % and a maximum partial current density of 1.2 A/cm^2. This newfound understanding of the relationship between particle size, crystallinity, and the novel reaction mechanism on nanoclusters opens new possibilities for designing superior catalysts that enable the production of previously unattainable products using conventional catalysts with larger particles.

2. Experimental section

2.1. Materials and chemicals

Electrochemical experiments were performed using a custom-built three-chamber flow-cell electrolyzer (illustrated in Fig. S1). The anion exchange membrane utilized was Fumasep (Fumatech). The reference electrode was an Ag/AgCl electrode (3 M KCl, Sigma Aldrich) and the counter electrode was made of nickel foam or platinum plate (Corrtest Instruments Co.) in the three-electrode configuration. The working electrode substrate was a gas diffusion carbon paper (YLS-30T, purchased from ʃFutt) that was used to deposit the Cu-based catalyst material. The catalyst and flow-cell were cleaned using RO water before and after each experiment. The electrolytes used were solutions of different concentrations of KOH (Sigma Aldrich) and KCl (Sigma Aldrich).

2.2. Physiochemical characterization

The morphology of the catalyst surface was characterized using ultra-high-resolution field emission scanning electron microscopy (Hitachi, Cold FE SU-8000 SEM) operating at a voltage of 30 kV. The elemental composition of the catalyst was determined using energy-dispersive X-ray spectroscopy (EDX). The oxidation state and binding energy on the catalyst surface were investigated using X-ray photoelectron spectroscopy (Thermo-Scientific, K-Alpha XPS apparatus) equipped with an Al K source. The X-ray spot size used was 400 μm, and the analysis chamber was maintained at a base pressure of approximately 10^{-7} bar. The C1s peak at 284.8 eV was utilized for energy referencing. The transmission electron microscopy (TEM) analysis was performed using the Talos F200X G2 S/TEM. Dry atomic force microscopy (AFM) was conducted using a MultiMode8™ SPM coupled with a Nanoscope™ V controller, both manufactured by Bruker in Santa Barbara, CA. We acquired all images using the ScanAsyst mode in ambient conditions, employing AC160TS cantilevers with nominal values as follows: Tip radius—9 nm, Resonant frequency—300 kHz, Spring constant—42 N/m, sourced from Asylum Research.

2.3. Ex-situ and in-situ XAS measurements

The Soft X-ray Microcharacterization Beamline (Canadian Light Source, SXRMB) was utilized for X-ray absorption spectroscopy (XAS) under ambient conditions, aimed at determining the atomic environment and oxidation states of the elements in the catalyst. The solid-state end-station under vacuum was used for the ex-situ measurements, while in-situ measurements were conducted using the ambient Table end-station. The latter measurements were performed using a modified flow cell, as depicted in Fig. S2. The XAS calibration was carried out using a Cu foil as the standard reference sample. The Extended X-ray Absorption Fine Structure (EXAFS) data collected was analyzed using the ATHENA software package, following standard procedures. The quantitative structural parameters around the central atoms were determined through least-squares curve parameter fitting performed using the ARTEMIS software.

2.4. Raman spectroscopy

Raman Spectra were collected using a Renishaw Invia Reflex system with a 633 nm laser having a 5 mW output power. Typically, the spectra were collected at full intensity power with a collection time of 60 seconds per spectra. The laser line focus illumination technique was also used which spreads the laser intensity out over a line to minimize the power concentrated on any particular spot, by approximately by 20–30X. For in-situ measurements, a three-electrode, GDE half-cell configuration was employed and a water immersion objective (numerical aperture of 0.7, working distance of 1 mm) was used to maximize signal intensity. The objective focused on the surface of the electrode where the catalytic gas-liquid-solid interfaces were located. In this system consisting of an Ag/AgCl reference electrode, Ni Foam counter electrode and 0.25 M KOH or KOD as electrolyte under a constant CO_2 or N_2 flow. The gas was flown through at approximately 20 sccm to maintain a steady reactant supply. For the working electrode either 100 nm Cu or Cu NC on gas carbon paper GDEs was used. Spectra were first taken at open circuit, then under increasingly negative applied current densities.

2.5. Preparation of electrodes

A gas diffusion carbon paper (YLS-30T) served as the substrate for the experiments. Copper, with 99.9999 % purity obtained from Angstrom Engineering, was sputter deposited onto the substrate using the NexDep Ebeam Evaporator (Angstrom Engineering Inc.) at a deposition rate of 0.5 Å/s for thin samples (<5 nm) and 1 Å/s for thick samples (between 5 nm and 100 nm), for varying thicknesses, under a vacuum pressure of 6×10^{-6} torr. For the 200 nm sample, a 100 nm layer was deposited followed by a 10-minute break before depositing the next 100 nm layer. During the experiments, a platinum plate was used as the anodic electrode when the electrolyte contained KCl, while a nickel foam was used as the anodic electrode in other cases.

2.6. Electrochemical measurements

Electrochemical evaluations were performed in a three-chamber flow cell consisting of a CO_2 gas chamber, a cathodic chamber, and an anodic chamber separated by an anion exchange membrane (as depicted in Fig. S1). Leak-proof sealing was achieved by utilizing PTFE gaskets between each component and tightening the cell with bolts and knots. A piece of nickel foam served as the anode electrode when KOH electrolyte was used, while a platinum plate was the anode electrode when a mixture of KOH and KCl was used as the electrolyte. All electrochemical measurements were performed using an Autolab potentiostat (PGSTAT 204, equipped with a current booster 10 A). The reference electrode was Ag/AgCl in 3 M KCl and all potentials were converted to the reversible hydrogen electrode (RHE) scale using the following equation:

$$E(RHE) = E_{Ag/AgCl} + 0.210V + 0.0591 \times pH - 0.85 \times iR$$

The ohmic loss between the working and reference electrodes was measured using the electrochemical impedance spectroscopy (EIS) technique (Table S3), and an iR compensation factor of 85 % was applied to correct potentials versus RHE. The EIS measurements were conducted with KOH and KOH + KCl electrolytes of varying concentrations, with an amplitude of 5 mV from 10^{-1} to 10^5 Hz. During the chronopotentiometry (CP) tests, the anolyte and catholyte were circulated through the anodic and cathodic chambers, respectively, using peristaltic pumps with a flow rate of approximately 10 ml/min. Continuous purging of CO_2 gas was maintained in the gas chamber at a flow rate of 80–100 sccm. The outlet flow rate was monitored using a mass flow controller calibrated by CO_2 gas.

2.7. Product analysis

Gas product analysis was conducted via GC-FID with a methanizer for CO, ethylene, and ethane quantification. The GC was calibrated by a standard gas cylinder (Fig. S3). The gas outlet from the flow cell was directly connected to the GC instrument using gas-tight connectors and copper tubing. During the GC process, the instrument automatically sampled 1 ml of gas from the tubing to generate a gas chromatograph.

The gas analysis employed a Clarus 590 GC with dual columns, utilizing argon as the carrier gas. Column 1 was a HayeSep N column, and column 2 was a MoleSieve 13X. A modifiable restrictor valve directed gas flow between the columns. Initially, gases traveled through column 1, followed by trapping in column 2. At 1.20 min into the runtime, the GC shut column 2 with the restrictor valve, capturing faster gases. Slower gases bypassed column 2 and reached the thermal conductivity detector (TCD). At 5.05 min, the valve reverted, and gases in column 2 were analyzed. Post-TCD detection, gases are mixed with H_2 and entered the methanizer, where C-based gases are converted to methane before proceeding to the Flame Ionization Detector (FID).

The liquid products were analyzed using a high-performance liquid chromatography (HPLC) on a Thermo Ultimate 3000 instrument with a Rezex ROA-Organic Acid H+ (8 %) column. The HPLC was calibrated by different CO_2RR liquid products (Fig. S4). The mobile phase consisted of 0.005 N sulfuric acid. To examine the liquid products from the electrochemical tests, 3 ml of 1 N sulfuric acid was added to 5 ml of the liquid sample, which was then sonicated for 15 min to remove any dissolved CO_2 gas. The sample was finally filtered through a syringe filter. In addition, nuclear magnetic resonance (NMR) spectroscopy was utilized to confirm the HPLC results.

2.8. Computational details

The copper nanoparticles (NPs) are built using the Wulff construction method [46] implemented in the atomistic simulation environment (ASE) code [47]. Density functional theory (DFT) calculations are performed using CP2K [48]. The cut off energy was determined with an appropriate convergence test and is set to 550 Ry. The simulation box is set so the nanoparticles are effectively isolated. The exchange correlation functional used is Perdew–Burke-Ernzerhof (PBE) for unit cell optimization and for lone nanoparticles. For unit cell optimization, the Monkhorst-Pack scheme is used and $8 \times 8 \times 8$ k points are used. The smearing and mixing method used are Fermi-Dirac [49] and Broyden mixing [50]. The basis sets and potentials used are DZVP-MOLOPT and GTH-PBE. Unit cell optimization is first performed to get the lattice parameter of copper found at 3.651 Ang. Then, nanoparticles are created by varying the surface miller indices and size (number of atoms). A full list of the nanoparticles simulated is available in Table S1. For nanoparticles with adsorbates, the PBE-D3 Grimme functional [51] is used to take into account van der Waals forces. Furthermore, because the Cu (111) nanoparticle is small at 19 atoms, the atoms are fixed to preserve

the structural integrity of the catalyst without having to add a support, which would require much more computational power. A deeper explanation on each computational parameter can be found in the following paper [52].

DFT computations on slabs were performed using Vienna Ab initio Simulation Package (VASP) [53–55] and calculations were run over the servers provided by Compute Canada. All calculations used projected augmented wave (PAW) pseudopotentials and Perdew-Burke-Ernzerhof (PBE) [56–59] as their exchange approximation correlational functional. A 4×4×1 grid of Monkhorst-Pack electronic wavevector was implemented in all calculations. Plane-wave basis in all calculations included a planewave kinetic energy cut off of 400 eV. In both Cu(100) and Cu(111) slabs, we included four layers of copper atoms with the two bottom layers fixed to represent the bulk. All structure optimizations in VASP were conducted with the incorporation of the Grimme method of DFT-D3 by activating the IVDW tag in the INCAR files.

Using the following equation, we calculated the excess energy for every created particle:

$$E_{Excess} = \frac{E_{nanoparticle} - N * E_{fcc-Cu}}{N} \qquad (1)$$

Where $E_{nanoparticle}$ is the optimized DFT energy of the nanoparticle, N is the number of atoms of the nanoparticle, and E_{fcc-Cu} is the energy per atom of the optimized FCC unit cell of copper.

3. Result and discussion

DFT computations have been substantially used in literature to shed light on the reaction mechanism and guide the catalyst design. A large portion of studies on copper catalysts are focused on crystalline surfaces using the slab model, representing a large bulky material [60–64]. Extremely small nanoparticles (NPs), known as nanoclusters (NC), cannot be represented using the slab model due to the absence of the periodic boundary condition applicable to slabs but not isolated particles. While creating a surface with a specific crystalline facet using the slab model is straightforward, generating particles with multiple facets presents various possibilities. In this study, we employed Wulff's construction method [65] to create particles of each nominal size, considering all combinations of four stable low-index facets: (111), (100), (110), and (221), with varying surface energy ratios. To assess surface stability, surface energy calculations are commonly used. However, surface energy depends strongly on surface area, which is ill-defined for NPs with complex shapes. Instead, we employ excess energy (Eq. 1), which relies solely on the number of atoms or size, to evaluate the stability of each created NC [66].

Fig. 1 presents excess energy curves for pure Cu(111), Cu(110), and Cu(100) among the numerous simulated nanoparticles, allowing for stability comparisons at various sizes. High-accuracy power-law trendlines are fitted to these curves (R^2 = 0.9998–0.9999). The results indicate that single-crystal Cu(111) NCs (diamond shape) exhibit greater stability than single-crystal Cu(100) NCs (cubic shape) at small sizes. Notably, the power-law trendline suggests that this trend may change with increasing particle size. However, due to the limitations of DFT, simulating NPs with 500+ atoms are computationally intensive and time-consuming. Consequently, we cannot definitively confirm whether Cu(111) NPs are less stable than Cu(100) NPs at larger sizes. Cu(110) NCs were also simulated and included in Fig. 1, illustrating slightly higher stability than Cu(100) but still considerably less stable than Cu(111).

We created other NCs with varying ratios of Cu(110) and Cu(221) surfaces, as well as NCs containing a combination of different facets. To evaluate their stability, any points above the Cu(111) trendline are deemed unstable. Notably, the only NCs found below the Cu(111) trendline are those with a combination of both Cu(111) and Cu(100) surfaces. Interestingly, at small sizes (<100 atoms), only NCs primarily
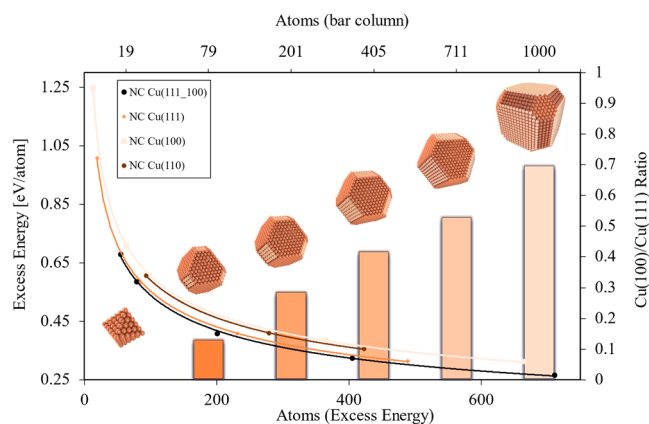

Fig. 1. Excess energy curves for pure Cu(111) NCs, pure Cu(100) NCs, and NCs with a combination of both. The Cu(100)/Cu(111) ratio is shown as bar columns with the appropriate axis on the right. A NC schematic that is increasing in size shown on top of the graph and matches each bar column. DFT results revealed that Cu(110) only appears at larger particles, as constructing small crystals with this facet is not feasible.

composed of Cu(111) with a small Cu(100) component are more stable than pure Cu(111). This observation supports the hypothesis that as size increases, the stability of the diamond-shaped Cu(111) facet diminishes relative to the more rounded football-shaped particles composed of Cu (111) and Cu(100). As the number of atoms increases, the ratio of Cu (100) to Cu(111) facets also increases. Although this assumption cannot be confirmed due to computational limitations in DFT, we propose that at very large sizes, the most stable nanoparticles feature a combination of (100), (111), and (110) facets, forming a polycrystalline particle, as illustrated by the largest NP in Fig. 1.

We synthesized copper particles with nominal sizes ranging from 0.5 nm to 200 nm on a carbon paper gas diffusion layer (GDL) support using an electron beam (e-beam) evaporator. Scanning electron microscopy (SEM) images in Fig. 2A and high-angle annular dark-field (HAADF) images (Fig. S5, S6) reveal that in the case of the sputtered 1 nm Cu deposition on the support, numerous extremely small particles are observed, and the GDL exhibits non-conformal coverage. In contrast, as the nominal size of the sputtered copper increases to 200 nm, the Cu particles grow in size, resulting in complete coverage of the GDL. It should be emphasized that the nominal sizes reported do not strictly align with the actual particle sizes observed. Our detailed analysis of the grain size distribution, as shown in Fig. S7, establishes a clear correlation between the nominal and the actual sizes of the particles. This finding indicates that despite the discrepancy between nominal and actual sizes, an increase in the nominal size consistently leads to an increase in the actual size. Energy dispersive X-ray (EDX) analysis (inset of Fig. 2A) indicates that the Cu particles exhibit uniform dispersion on the surface in thinner samples and full coverage in thicker ones. Furthermore, atomic force microscopy (AFM) images of the Cu nanoclusters (Fig. S8) also illustrate a consistent and distinct distribution of Cu nanoclusters, with uniform height observed across the sample.

As evidenced by the selected area electron diffraction (SAED) images and high-resolution transmission electron microscopy (HRTEM) depicted in Fig. 2B-2C and Fig. S9, thinner samples (< 2 nm) exhibit the exclusive presence of Cu(111) facets. However, as the particle size increases, the proportion of Cu(111) facets decreases while other facets become increasingly prominent, aligning with the findings from our DFT computations. We conducted an extended X-ray absorption fine structure (EXAFS) analysis to probe the local structure of copper (details provided in Fig. 3A, Fig. S10-S12 and Table S1). In accordance with the findings in the literature [17], it is observed that as the size of the sputtered copper particles decreases, the metallic Cu-Cu bond coordination number correspondingly diminishes. For instance, the smallest
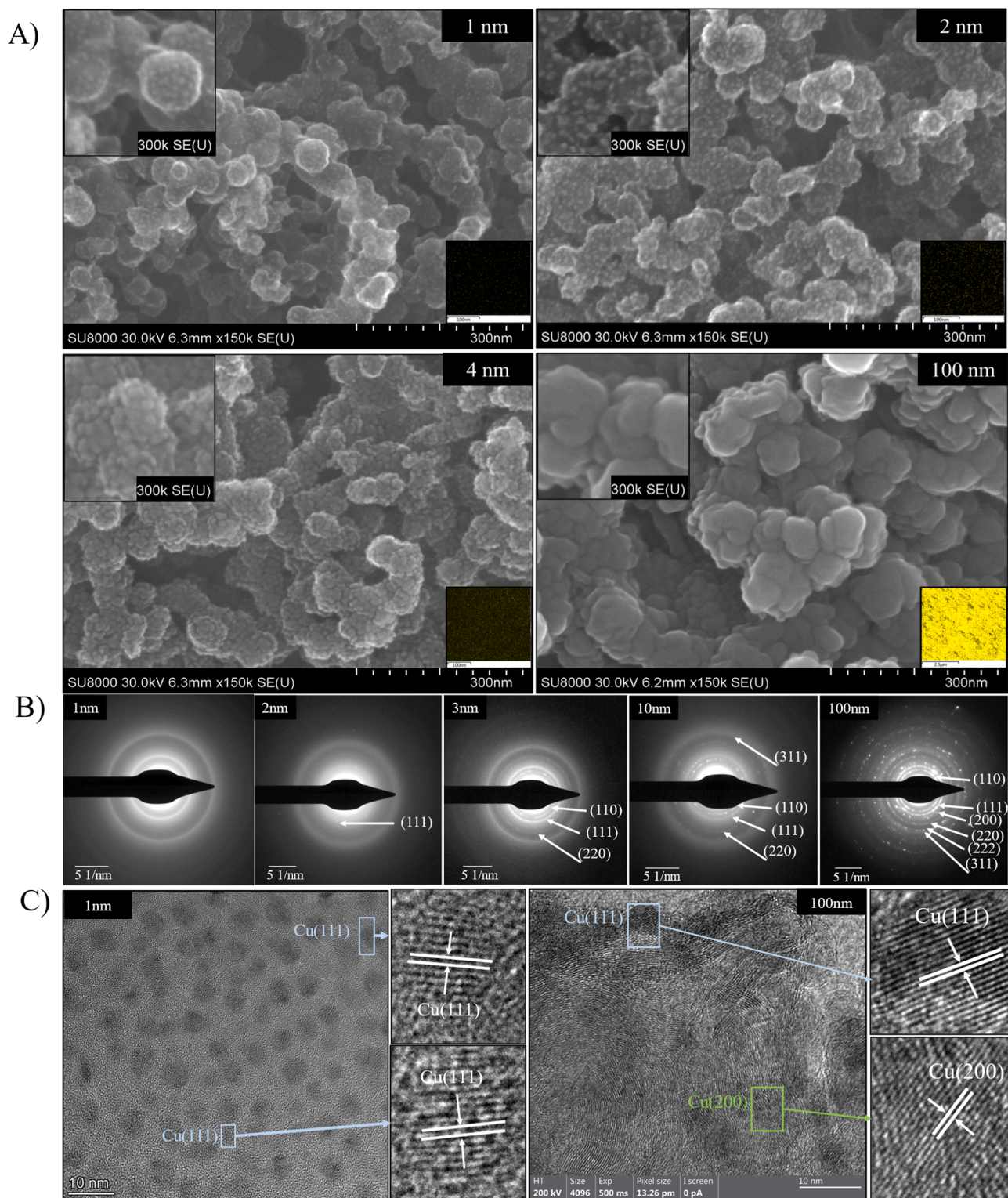
Fig. 2. A) SEM images, B) SAED patterns, C) HRTEM images of Cu nanoparticles with different sizes.

synthesized particle (0.5 nm) exhibited a Cu-Cu bond coordination number of 1.8, whereas a larger sample (100 nm) displayed a coordination number of 7.3. To provide a more comprehensive analysis of the surface composition, we employed high-resolution X-ray photoelectron spectroscopy (XPS) and Auger electron spectroscopy (AES) to examine the Cu 2p and Cu LMM spectra (Fig. 3C-D, S13). Deconvolution of the high-resolution XPS spectrum in Fig. 3C reveals two prominent peaks at 933.1 eV and 935.7 eV, corresponding to Cu^{2+} (CuO) and CuF_2,

respectively, within the small particles. The presence of strong satellite peaks at 943 eV further confirms the presence of higher oxidation states (Cu^{2+}) in these particles. In contrast, the larger particles (as shown in Fig. 3D) primarily exhibit a Cu^0/Cu^+ state with a dominant peak at 932.5 eV and a notable absence of strong Cu^{2+} satellite peaks, indicating less oxidized Cu in comparison to the smaller particles. The subsequent AES (Fig. S13) investigation concurred with these interpretations, displaying peaks at 918.6, 916.6, and 918.2 eV corresponding to Cu^0, Cu^+,
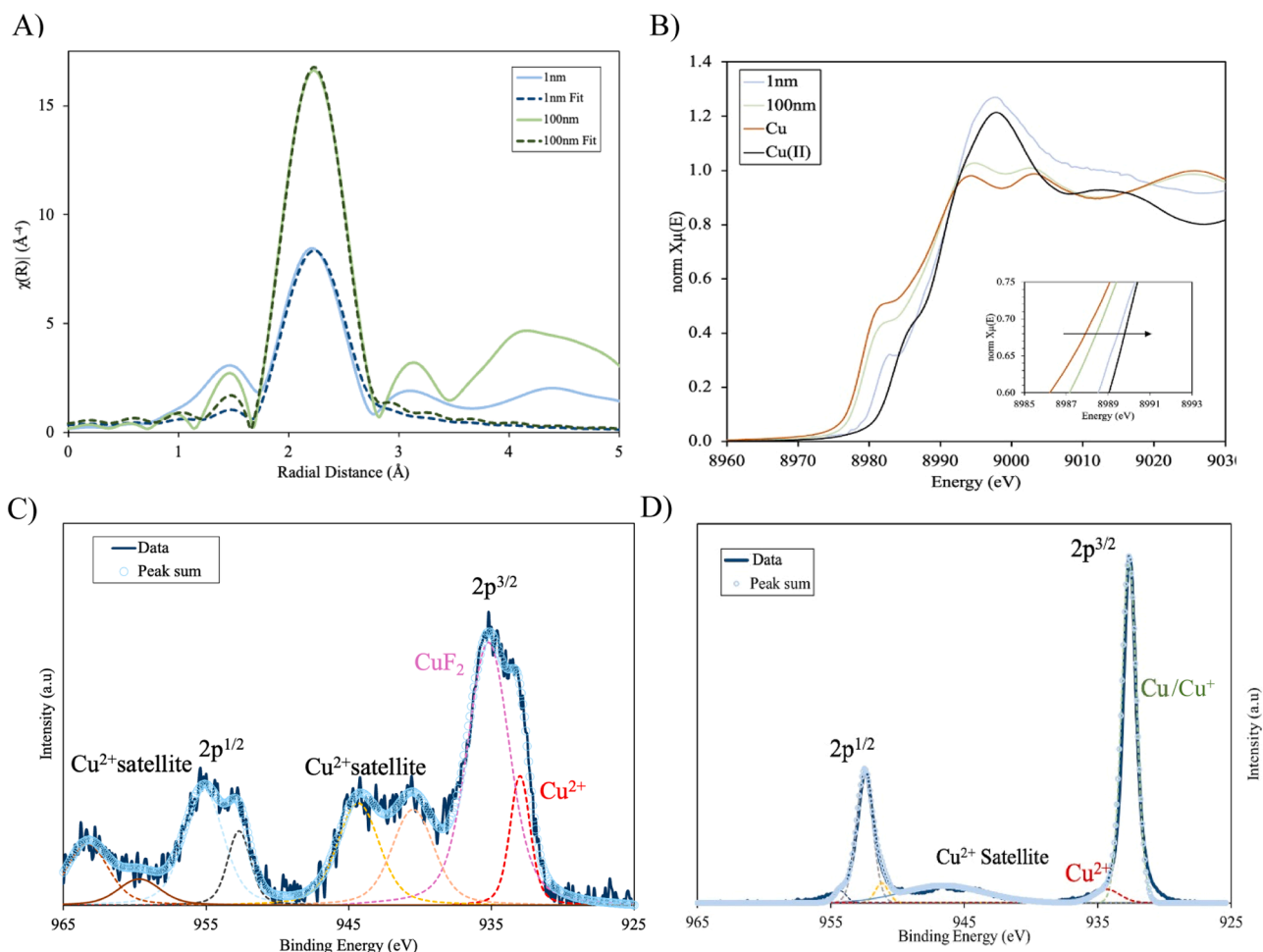
Fig. 3. A) EXAFS, B) XANES data of 1 nm and 100 nm Cu catalysts. XPS spectra of C) 1 nm D) 100 nm Cu catalyst.

and Cu^{2+}, respectively, consistent with established literature [67]. Specifically, the 100 nm sample's peaks at 918.6 and 916.6 eV indicate the simultaneous presence of Cu^0 and Cu^+, mirroring the XPS findings. Meanwhile, a distinctive peak at 915 eV in the 0.5 nm sample corroborates the presence of CuF_2, underpinning the proposed higher oxidation state. Furthermore, the X-ray absorption spectroscopy near-edge spectra (XANES) of copper, as presented in Fig. 3B, exhibit a rising edge at approximately 8988 eV, suggesting a higher degree of oxidation for the Cu species near the surface of the smaller particles compared to the larger ones. Comparative analysis of the first derivatives of XANES spectra for 1 nm and 100 nm copper samples reveals a higher oxidation state in the thinner sample (Fig. S14). This observation aligns with XPS analysis, underscoring the influence of particle size on the oxidation state of copper. These observations align with our expectations, as a greater proportion of copper atoms is exposed to air in the thinner sample compared to the thicker one. Consequently, a higher degree of oxidation in the copper species is observed in the thinner sample. Although ex-situ characterization of the NCs suggested the presence of higher oxidation states for copper, our in-situ XANES measurements consistently indicate that the thickness of the copper samples has no apparent impact on the reduction of copper to its elemental state, Cu^0, when subjected to a negative current (Fig. S15). As a result, we have opted to employ Cu^0 as the catalyst in our DFT simulation.

The DFT results summarized in Fig. 1, coupled with the characterizations of the synthesized particles presented in Fig. 2, substantiate the hypothesis that copper nanoclusters with exceedingly small particle sizes (e.g., 6.4 Å, equivalent to approximately 19 atoms), predominantly consist of Cu(111) facets, while larger particles (e.g., 100 nm) are expected to exhibit a more substantial contribution from Cu(100) facets. Consequently, it is imperative to investigate and compare the CO_2RR mechanism towards C_1 products (e.g., methane) and C_2 products (e.g., ethylene) using two distinct models: (*i*) the extremely small Cu(111) NCs and (*ii*) the Cu(100) slab, representing particles synthesized at exceedingly small and large sizes, respectively.

Fig. 4 provides an overview of the reaction mechanism for the CO_2 reduction to methane and ethylene on an extremely small Cu(111) NC. Similar computations have been conducted on slab models to represent larger particles with various facets. Detailed computational procedures and results for these slab models can be found in the supplementary information (refer to Fig. S16-S18 for reference).

When comparing the reaction pathways on these two distinct models, several noteworthy differences come to light. The first intriguing observation pertains to CO_2 adsorption on the catalyst. While CO_2 forms a weak physisorption bond with the surface of Cu slabs (Fig. S16), it undergoes strong chemisorption on the Cu(111) NC with 19 atoms, exhibiting a favorable adsorption energy of −0.170 eV. Notably, as the size of the Cu NC increases to include 79 atoms, we observe an unfavorable CO_2 adsorption energy of +0.19 eV [68], indicating that the smaller NCs indeed enhance the adsorption process. Consequently, a facile CO_2 activation step is anticipated during the CO_2RR on these NCs. The stronger chemisorption of the CO_2 molecule on smaller Cu NCs can be attributed to the lower coordination number of the NCs, as confirmed by the EXAFS results. This, in turn, underscores their greater reactivity. Remarkably, CO_2 is adsorbed through the oxygen atom onto the Cu NCs, in contrast to the more common adsorption through the carbon atom observed on Cu slabs (Fig. S17), indicating a drastic difference in CO_2RR
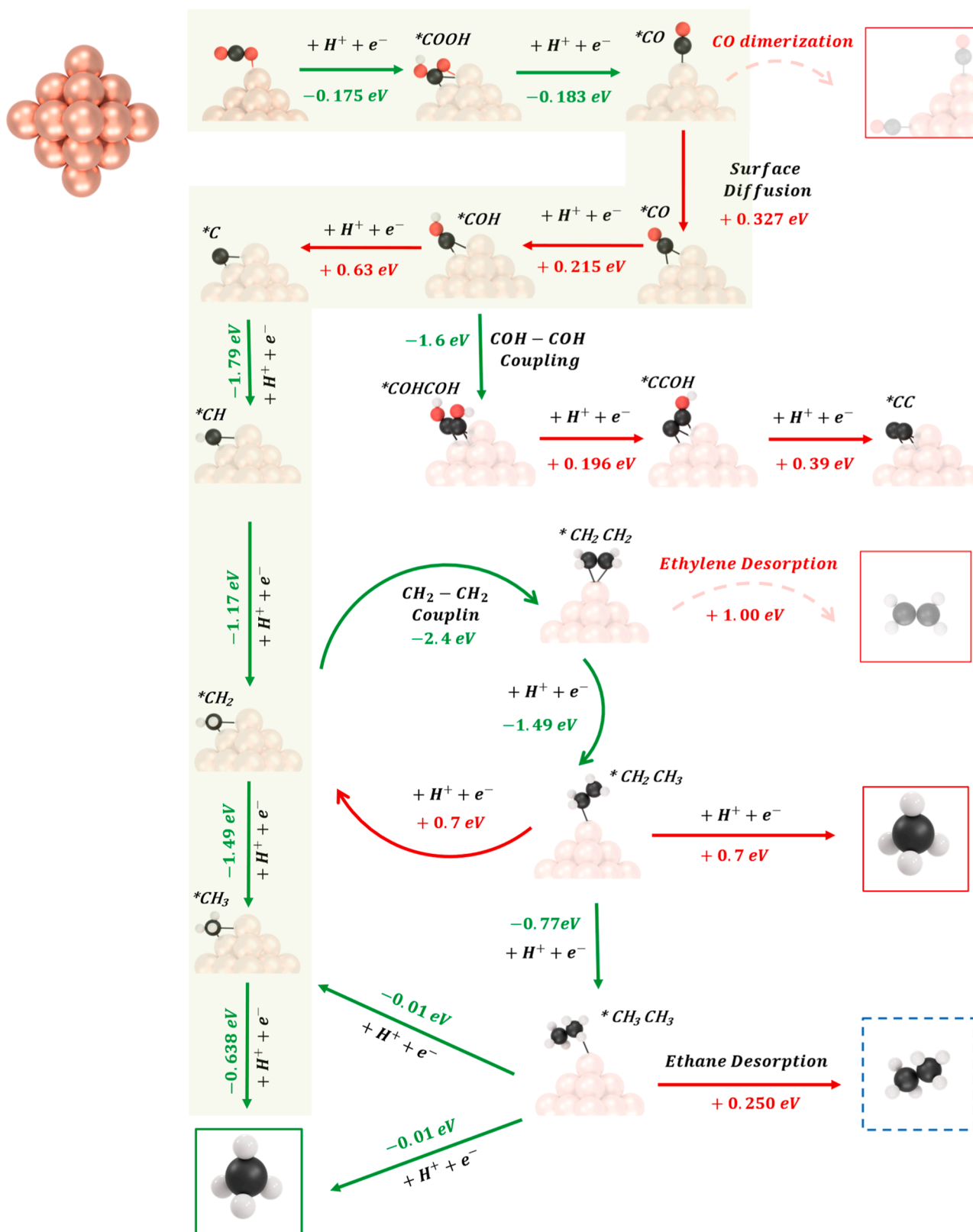
Fig. 4. Overall mechanism from CO_2 to CH_4 including unfavorable side reactions, C-C uncoupling, and re-routing. For each elementary step, the energy difference is shown and is in green if negative (favorable) and red if positive (unfavorable). The highlighted pathway is the most favorable pathway for CH_4 formation.

mechanism on NCs compared to larger particles. This unique adsorption occurs at the apex atom of the Cu NC pyramid, which exhibits the lowest coordination number among all the constituent Cu atoms within the NC (Fig. 4). In the case of the 19-atom Cu(111) NC, there are two such apex

sites at the top and bottom of the pyramid. These two sites have proven to be pivotal in the reaction mechanism due to their distinctive coordination environment, which differs from that of a typical bulk copper atom.

Both the protonation of CO_2 to *COOH and the protonation of *COOH to the adsorbed *CO are found to be exergonic on Cu NC at −0.175 eV and −0.183 eV, respectively. While *CO is typically adsorbed on the bridge site of Cu slabs [69,70], we observed that on Cu NC, it is adsorbed on the top site of the apex atom of the pyramid. Notably, adsorption on this top site is found to be 0.32 eV more stable than the bridge site.

On the Cu(111) slab, multiple studies in the literature have demonstrated that *COH is the favored product of *CO protonation, as opposed to *CHO [62,69–72]. This preference has been attributed to the interaction between *COH and water molecules in the electrolyte, which significantly stabilizes the *COH intermediate. It is suggested that protonating the oxygen atom rather than the carbon atom is the preferred route. Furthermore, *CHO is formed through surface hydrogenation by an adsorbed hydrogen (*H) [69,70]. In our investigation, similarly, we observed that the inclusion of explicit water molecules substantially stabilizes the *COH intermediate through hydrogen bonding, shifting the selectivity towards *COH, as summarized in Fig. S19.

In the formation of *COH, we consider an *H_5O_2 complex as the proton carrier. Initially, the top *CO relocates to the bridge position, with an associated energy barrier of 0.32 eV. Subsequently, the protonation of the bridge *CO by the *H_5O_2 complex leads to the adsorption of two water molecules, resulting in a bridge/hollow *COH intermediate. The reaction energy is calculated to be 0.215 eV. Considering the initial diffusion step, the overall reaction energy for the protonation of *CO to *COH is determined to be 0.54 eV. Similar mechanism for the formation of *CHO deemed unfavorable as the energy barrier to hydrogenate the carbon in *CO from a proton in solution is very high [62, 69,70,73]. Conversely, in the formation of *CHO, we consider an adsorbed *H near the top *CO. In this case, the reaction energy is found to be 0.613 eV, which is higher than that for the formation of *COH. Production of *COH by surface hydrogenation of *CO with an adsorbed *H is also unfavorable at an energy difference of +1.66 eV. Furthermore, previous studies have also demonstrated that when *COH is formed, the predominant product is methane, primarily attributed to the favorable *COH to *C transition, in a similar manner to the *CO hydrogenation [62,72]. Conversely, in cases where *CHO is produced, methanol can be generated through the hydrogenation of carbon to reach the *OCH_3 intermediate, leading to the formation of CH_3OH [62,72].

On the Cu(100) slab, the *CHO formation is favored over the *COH. The reaction energy for the protonation of *CO to *CHO and *COH are found to be 0.397 eV and 1.43 eV, respectively. Furthermore, our calculations reveal that the dimerization of *CHO (i.e., *CHO-CHO) is highly exergonic at −1.50 eV on the Cu(100) slab, which significantly enhanced the production of multicarbon (C_{2+}) products. To further investigate other C-C coupling pathways, we also considered the dimerization of *CO, *COH, *CHO, and *CH_2 on the Cu NC. Our findings indicate that *CO-CO coupling does not occur on Cu NC, as shown in Fig. S20. However, it is feasible on the Cu(100) slab, with an associated reaction energy of 0.979 eV, consistent with the findings in the literature [41,74–76]. The *COH-COH coupling is possible on Cu NC. Nevertheless, our subsequent analysis demonstrates that, even after C-C coupling, methane remains the preferred product. The *CHO-CHO coupling is exclusively possible on the Cu(100) slab, as previously explained, and is not observed on Cu NC due to the high reaction energy associated with placing *CHO on the surface. Consequently, the sole remaining potential C-C coupling pathway is *CH_2 dimerization, which leads to the production of ethylene (C_2H_4). The selectivity of *CH_2 dimerization pathway, in contrast to its protonation to *CH_3 and subsequently to methane, depends on various influencing factors, including the surface coverage of *CH_2 and the applied potential [41,62,72]. Our experimental results, as discussed below, reveal the absence of any detectable ethylene production at any potential when using the smallest synthesized Cu NC (i.e., 0.5 nm), with methane emerging as the predominant product. As a result, we postulate that even if two *CH_2 intermediates were to couple on the surface of the Cu NC, the reaction pathway would

shift towards methane in the subsequent reaction steps.

One of the most intriguing distinctions between Cu NC and Cu slab is the behavior of ethylene desorption. Our DFT calculations reveal that ethylene interacts with the apex atom of Cu NC, resulting in a relatively high adsorption energy of *CH_2CH_2 at 1.03 eV. As a point of comparison, this energy is 0.287 eV on Cu(100) and 0.148 eV on Cu(111) slabs (Table S2). This observation prompted the hypothesis that *CH_2CH_2 will undergo further reduction instead of desorbing as a product. The reduction process is detailed in Fig. 4, which illustrates the conversion of *CH_2CH_2 to *CH_3CH_2, subsequently to *CH_3CH_3 (ethane), with the possibility of either ethane desorption or its decoupling into CH_4 and *CH_2. The desorption of ethane is associated with a reaction energy of 0.25 eV higher than that of methane production. Consequently, the remaining *CH_2 can be readily reduced to CH_4 or engage in the same "C-C uncoupling" cycle, irrespective of external factors such as the applied potential. The only remaining plausible pathway that can potentially result in ethylene formation is through the coupling of *COH-COH, a highly exergonic reaction with an energy release of −1.6 eV. However, the *COH-COH intermediate produced is more likely to undergo protonation through the oxygen atoms, primarily due to the presence of two -OH groups. Over two successive steps, this protonation process transforms the intermediate into *CC, which lacks any oxygen moieties. Consequently, the formation of products such as ethanol and acetaldehyde are precluded. Therefore, the *CC intermediate can only give rise to CH_2CH_2, which subsequently follows the C-C uncoupling process described earlier.

Furthermore, we explored other heterogeneous couplings, such as those involving *CH_x and *CO, which have received limited attention in the literature [77]. The possibilities for these couplings are summarized in Table S6. Specifically, *CO coupling with *CH and *CH_2 is feasible with associated energies of −1.09 and −0.49 eV, respectively. However, *CO coupling with *CH_3 proves unfavorable, entailing a reaction energy of 0.57 eV. Post-coupling protonation is expected to primarily occur through the carbon atoms due to the presence of the C=O double bond. Protonation of either the carbonyl carbon or the adjacent carbon results in similar outcomes, leading to the adsorption of *CH_3CHO. This species, *CH_3CHO, serves as a common intermediate for all the C_2 products considered in this study [77]. Subsequently, *CH_3CHO can desorb as acetaldehyde molecules. The pathways for forming acetaldehyde and ethanol, along with their associated desorption energies, are summarized in Table S7. Both acetaldehyde and ethanol exhibit desorption energies of 0.4 eV, which is higher than the energies required for subsequent protonation steps. These protonation steps yield *C_2H_X species, which subsequently undergo the C-C uncoupling process.

The sputtered copper catalysts, synthesized with thicknesses spanning from 0.5 nm to 200 nm, were tested under CO_2RR conditions within a flow cell setup. The pathway towards ethane formation was validated by GC-FID results, as illustrated in Fig. 5A. These results revealed the presence of a detectable quantity of ethane (< 5 ppm) when utilizing the Cu NC (0.5 nm) catalyst. Conversely, no ethane was detected when larger Cu particles (200 nm) were employed under similar conditions. To validate the source of ethane as a product of CO_2 reduction rather than an impurity, we conducted a control experiment in which all parameters were held constant, except for the absence of reduction potential. In addition, we performed a control experiment to exclude the possibility of ethane formation from the carbon electrode, confirming that no ethane was detected with Cu NC without feeding CO_2 as the reactant. Fig. 5A illustrates that under these conditions, no ethane peak was detected. Additionally, it was observed that an increase in temperature from room temperature to 80 °C, corresponded to a rise in ethane production, owing to the enhanced desorption process at higher temperatures. Although this observation is not decisive as the temperature may affect various chemical steps in the reaction process too, slight increase in temperature found to be effective to overcome small desorption energy of ethane without affecting ethylene desorption with a larger desorption energy. This observation provides additional support
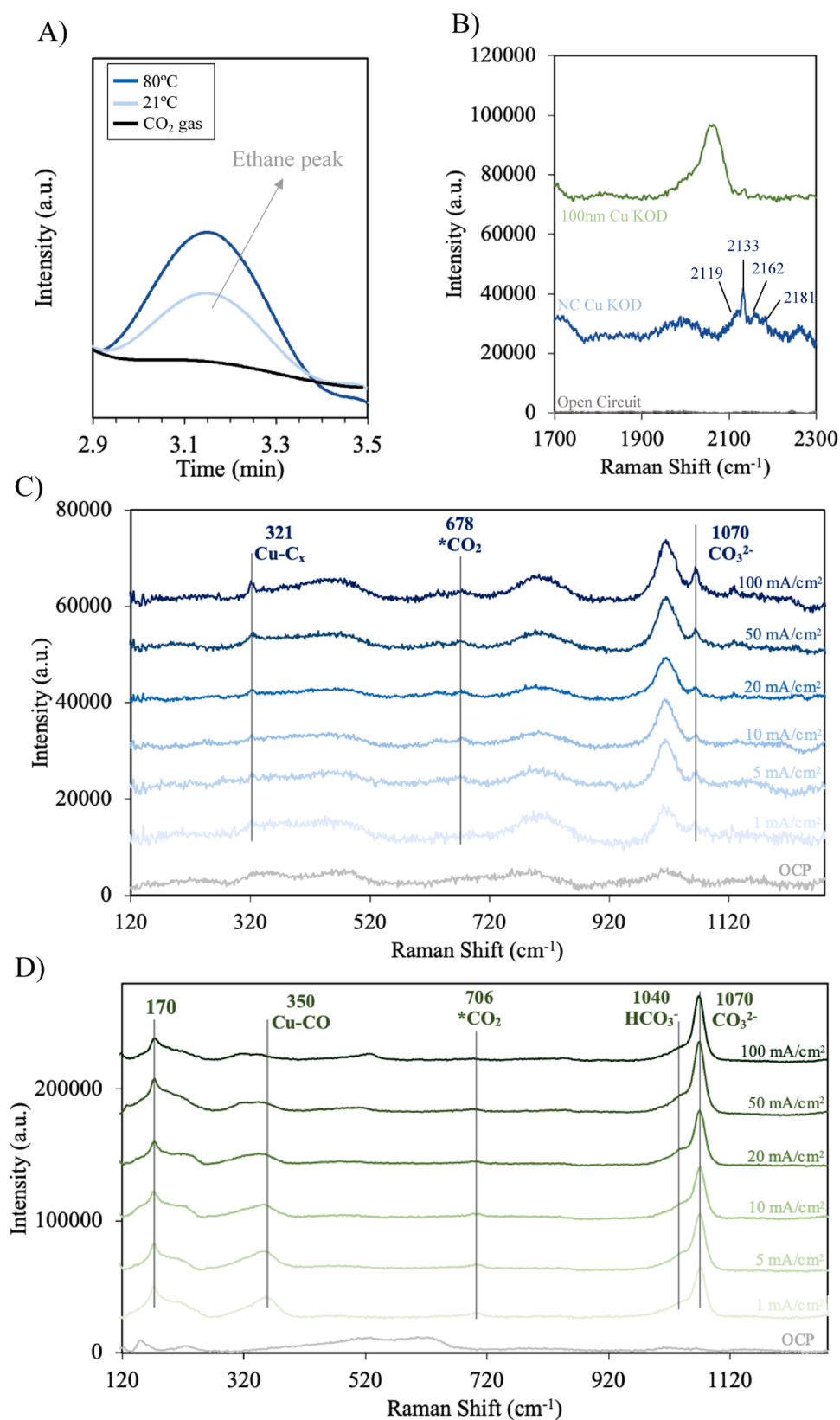
Fig. 5. A) Ethane peak in GC-FID at different temperatures on a 0.5 nm Cu NC catalyst. In-situ Raman spectroscopy results during the CO_2RR at B) Raman shifts between 1700 and 2300 cm^{-1}, C) Raman shifts between 120 and 1120 cm^{-1} for Cu NC catalyst and D) Raman shifts between 120 and 1120 cm^{-1} for 100 nm Cu catalyst.

for the synthesis of ethane facilitated by the Cu NC catalysts.

To correlate the hypothesized reaction pathway to an experimental observation of surface intermediates, we carried out operando Raman spectroscopy [78]. We focused our studies on two particular systems, Cu NCs and 100 nm thick films of Cu as a model system and point of reference. Under constant current conditions, the spectra on the 100 nm thick Cu catalyst revealed $*CO_{atop}$, $*CO_2^-$ as major intermediates, Cu-C bands, and CO_3^{2-} as a near-surface species (Fig. 5D). The shape of the $*CO$ band indicated that multiple different $*CO$ species are present, potentially on different active site configurations or featuring differing interactions with proximal surface species. This was similar to previous Raman studies on bulk Cu-based systems [79]. The results are also consistent with the notion that a high $*CO$ coverage is beneficial for ethylene production. The Cu NCs also featured $*CO_{atop}$, $*CO_2^-$ as major intermediates, though at much weaker intensity as the relative amount of catalyst was lower (Fig. 5C). The tentatively assigned Cu-C vibration was also blue-shifted relative to that of the bulk Cu (321 vs. 350 cm^{-1}), indicating differing binding types and energies. The tentatively assigned peak to $*CO_2^-$ was similarly blue-shifted (678 vs 706 cm^{-1}).

We then sought to investigate the presence of C-H containing species on the surface. The carbon paper electrode featured strong signals in this region, prohibiting us from accurately assigning peaks to surface-intermediates. However, when using D_2O/KOD as the electrolyte, the C-D bands were red-shifted to 2100–2300 cm^{-1} (Fig. 5B). When acquiring Raman spectrum in this region, the 100 nm Cu still showed

$*CO$ as the dominant species in the spectrum. In contrast, the Cu NCs exhibited C-D stretches, that indicated a higher prevalence of C-D containing surface reaction intermediates under catalytic conditions.

The CO_2RR experiments were conducted using a 0.25 M KOH electrolyte and at a current density of 300 mA/cm^2. As depicted in Fig. 6A, a pronounced trend emerges, showcasing the influence of particle size on CO_2RR product distribution, in line with DFT predictions. As the particle size decreased, a notable shift in the reaction pathway from ethylene to methane was observed. Notably, the Cu NC with a nominal size of 1 nm exhibited a high FE for methane, reaching 75 %—equivalent to a partial current density of 225 mA/cm^2. Remarkably, on the Cu NC with 1 nm nominal size, no detectable ethylene was observed, even at the high current density of 300 mA/cm^2. In contrast, catalysts with nominal sizes of 50 nm or larger showed no detectable methane, with ethylene emerging as the main gaseous product in line with existing literature [5, 31].

While the achieved current density for methane represents one of the highest reported results in the literature, we further enhanced the performance by optimizing the electrolyte concentration and utilizing even smaller Cu NC with a nominal sputtering size of 0.5 nm. As illustrated in Fig. S19, we observed that the FE for methane in a 0.25 M KOH electrolyte rises with increasing current density, reaching a peak FE of 76 % at a current density of 400 mA/cm^2. Subsequently, as the current density increases further, the FE gradually declines. This trend was consistent for more concentrated electrolytes, with the 0.5 M KOH electrolyte
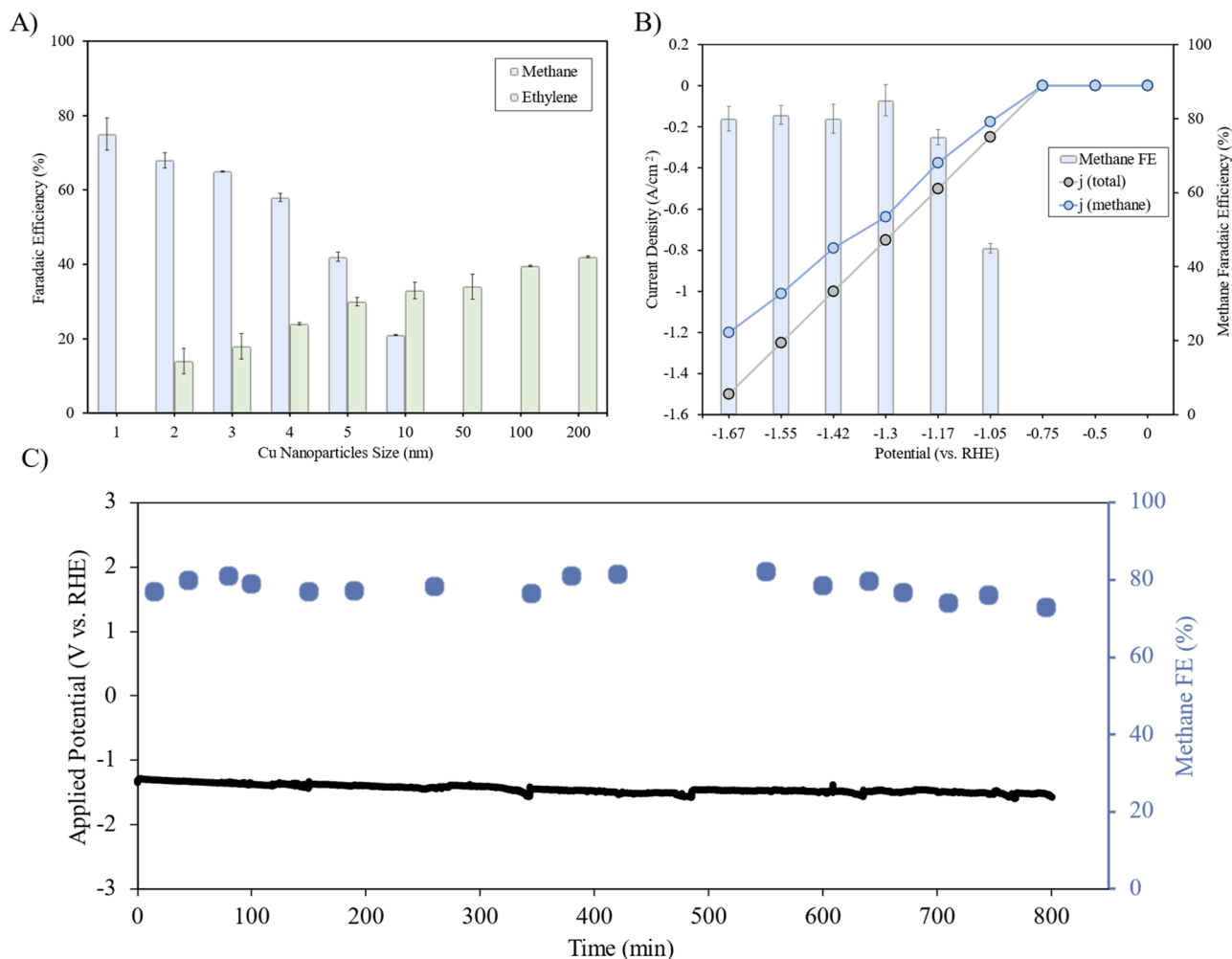
Fig. 6. A) Methane and ethylene FE for Cu nanoparticles with different sizes at 300 mA/cm^2 in 0.25 M KOH. B) Total current density and methane partial current density using a 0.5 nm Cu NC catalyst at different potentials in 1 M KOH + 2 M KCl. C) The extended CO_2RR performance using a 0.5 nm Cu NC catalyst in a flow cell at a constant current density of 200 mA/cm^2. A Pt electrode was used as the anode.

reaching a peak FE of 77.5 % for methane at a current density of 600 mA/cm^2, and with the 0.75 M KOH electrolyte achieving a maximum FE of 75 % for methane at 700 mA/cm^2. Hence, we postulated that high FE values for methane could be obtained at elevated current densities by increasing the alkaline electrolyte concentration. However, at current densities exceeding 1 A/cm^2, the HER becomes increasingly significant, limiting the ability to achieve a high FE for methane.

Inspired by prior studies [80,81], we embarked on an investigation into the impact of introducing potassium chloride (KCl) to the electrolyte (Fig. S20). This addition serves a dual purpose: augmenting the availability of essential potassium ions (K$^+$) crucial for the CO$_2$RR, while concurrently mitigating the undesired HER through the presence of chloride ions (Cl$^-$) that influence the interactions between reaction intermediates and electrode surfaces [82,83]. This exploration was conducted through linear sweep voltammetry (LSV) experiments under N$_2$ and CO$_2$ atmospheres, with varying pH levels and K$^+$ concentrations. Our observations revealed it did exhibit a notable effect on selectivity, shifting it away from the HER and towards the CO$_2$RR. These findings align with previous research, which postulates that within a proton-depleted local environment, the cation can stimulate CO$_2$ activation, consequently impeding the HER associated with water reduction [80,84,85]. Following the optimization of the electrolyte composition (1 M KOH + 2 M KCl), we achieved a remarkable maximum FE of 85 % for methane, obtained at a total current density of 750 mA/cm^2, using a 0.5 nm Cu NC catalyst. The highest partial current density for methane reached 1.2 mA/cm^2, corresponding to an FE of 80 % at a total current density of 1.5 A/cm^2. These results were achieved under an applied potential of −1.66 V versus the RHE, as depicted in Fig. 6B.

We then performed stability tests for the CO$_2$RR. While the gas diffusion electrode (GDE) is known for its high efficiency in CO$_2$RR [25, 27,86], it faces substantial challenges in terms of long-term stability, particularly when subjected to high current densities and harsh alkaline environments [87]. This stability issue is often attributed to the gradual loss of hydrophobic properties and eventual flooding of the GDE over time [27,31,88]. Given the remarkable FE achieved for CH$_4$ at a current density of 200 mA/cm^2 in a 0.25 M KOH solution, we opted to conduct the stability test under these specific conditions to postpone concerns related to catalyst flooding. The 0.5 nm Cu NC catalyst underwent testing in a flow cell, employing a 0.25 M KOH electrolyte and a current density of 200 mA/cm^2. As illustrated in Fig. 6C, the system exhibited stability for a duration of 2.5 hours, consistently maintaining an average FE of over 75 % for methane. However, a subsequent decline in the potential became apparent. To address this issue, the catalyst was subjected to a washing and drying process, followed by the resumption of CO$_2$RR using the same catalyst. This procedure led to the recovery of both the potential and the methane FE to their initial values. This outcome implies that the decrease in potential was likely a result of either carbonate salt accumulation on the catalyst's surface or substrate flooding. Through periodic washing and drying of the catalyst, stability was extended for a period exceeding 13 hours, with a consistently high average FE of over 75 %.

To address the structural stability of Cu NC catalysts following the CO$_2$RR, we conducted detailed post-CO$_2$RR characterizations. The STEM images confirmed the Cu NC nanoparticles remained anchored to the support material post-CO$_2$RR, indicating their physical stability (Fig. S21A). Moreover, the SAED analysis showed the Cu(111) facet remained predominant after the CO$_2$RR, highlighting the crystalline structure's stability, which is vital for the catalyst's activity and selectivity (Fig. S21B). The XPS results further confirmed the continued presence of copper post-CO$_2$RR (Fig. S21C).

4. Conclusions

In this study, we employed DFT computations to elucidate the stability of nanoparticles, particularly focusing on extremely small nanoclusters (NC), and to explore the underlying CO$_2$RR mechanism. Our findings revealed that at these extremely small sizes, Cu NCs with Cu(111) facets, adopting a pyramid shape, demonstrate the highest stability. As the particle size increases, other crystalline facets, notably Cu(100), contribute more, leading to the formation of a more rounded, football-like particle. We demonstrated that the CO$_2$RR pathway on Cu NCs diverges from those previously discussed in the literature utilizing slab models. Notably, owing to their low coordination number and higher reactivity, CO$_2$ and ethylene exhibit stronger chemisorption on the Cu NC. This strong chemisorption contributes to an enhanced CO$_2$RR, revealing a distinct preference for methane, and enabling subsequent protonation of ethylene leading to either ethane production or the initiation of a C-C uncoupling process that results in methane formation. *In-situ* Raman spectroscopy provided indirect evidence of the presence of the C-C bond on the Cu NC surface, indicating the adsorption of ethylene. Moreover, ethane was unequivocally detected through GC-FID on Cu NC, underscoring its distinctive capacity for protonating adsorbed ethylene in comparison to larger Cu particles. In our experimental efforts, we synthesized Cu nanoparticles of varying sizes, and it was evident that reducing the nanoparticle size shifted the selectivity from ethylene to methane, aligning with the predictions derived from DFT calculations. Furthermore, through the optimization of electrolyte concentration and composition, we demonstrated the feasibility of achieving high methane production, with a maximum FE of 85 % at 750 mA/cm^2 and a maximum partial current density of 1.2 A/cm^2, in alkaline environments.

CRediT authorship contribution statement

Nikolay Kornienko: Data curation, Formal analysis, Writing – review & editing. **Roger Lin:** Data curation, Formal analysis, Writing – review & editing. **Ali Seifitokaldani:** Writing – review & editing, Writing – original draft, Supervision, Conceptualization, Formal analysis, Funding acquisition, Methodology, Project administration, Resources. **Hasan Al-Mahayni:** Writing – review & editing, Writing – original draft, Visualization, Validation, Methodology, Formal analysis, Data curation. **Mahdi Salehi:** Writing – review & editing, Writing – original draft, Visualization, Validation, Methodology, Formal analysis, Data curation, Conceptualization. **Morgan McKee:** Writing – review & editing, Writing – original draft, Visualization, Formal analysis, Data curation. **Amirhossein Farzi:** Writing – review & editing, Writing – original draft, Visualization, Validation, Formal analysis, Data curation. **Elmira Pajootan:** Formal analysis, Writing – review & editing. **Sepideh Kaviani:** Data curation, Writing – review & editing.

Declaration of Competing Interest

The authors declare the following financial interests/personal relationships which may be considered as potential competing interests: Ali Seifitokaldani reports financial support was provided by Natural Sciences and Engineering Research Council of Canada. If there are other authors, they declare that they have no known competing financial interests or personal relationships that could have appeared to influence the work reported in this paper.

Data Availability

Data will be made available on request.

Acknowledgement

Appendix A. Supporting information

Supplementary data associated with this article can be found in the online version at doi:10.1016/j.apcatb.2024.124061.

References

[1] L. Jeffry, et al., Greenhouse gases utilization: a review, Fuel 301 (2021) 121017.
[2] R. Wang, et al., Engineering a Cu/Znox interface for high methane selectivity in CO_2 electrochemical reduction, Ind. Eng. Chem. Res. 60 (1) (2021) 273–280.
[3] C. Liu, et al., In Situ Reconstruction of Cu–N coordinated mofs to generate dispersive Cu/Cu2O nanoclusters for selective electroreduction of CO_2 to C_2H_4, ACS Catal. 12 (24) (2022) 15230–15240.
[4] T. Li, et al., Electrolyte driven highly selective CO_2 electroreduction at low overpotentials, ACS Catal. 9 (11) (2019) 10440–10447.
[5] C.M. Gabardo, et al., Continuous carbon dioxide electroreduction to concentrated multi-carbon products using a membrane electrode assembly, Joule 3 (11) (2019) 2777–2791.
[6] T.N. Nguyen, et al., Fundamentals of electrochemical CO_2 reduction on single-metal-atom catalysts, ACS Catal. 10 (17) (2020) 10068–10095.
[7] B. Zhang, et al., Steering CO_2 electroreduction toward methane or ethylene production, Nano Energy 88 (2021) 106239.
[8] S.-F. Hung, et al., A metal-supported single-atom catalytic site enables carbon dioxide hydrogenation, Nat. Commun. 13 (1) (2022) 819.
[9] S.-F. Hung, Electrochemical flow systems enable renewable energy industrial chain of CO_2 reduction, Pure Appl. Chem. 92 (12) (2020) 1937–1951.
[10] M.K. Kim, et al., Metal–organic framework-mediated strategy for enhanced methane production on copper nanoparticles in electrochemical CO_2 reduction, Electrochim. Acta 306 (2019) 28–34.
[11] A. Sedighian Rasouli, et al., Ga doping disrupts C-C coupling and promotes methane electroproduction on cual catalysts, Chem. Catal. 2 (4) (2022) 908–916.
[12] X. Wang, et al., Gold-in-Copper at Low *CO coverage enables efficient electromethanation of CO_2, Nat. Commun. 12 (1) (2021) 3387.
[13] Y. Li, et al., Promoting CO_2 methanation via ligand-stabilized metal oxide clusters as hydrogen-donating motifs, Nat. Commun. 11 (1) (2020) 6190.
[14] X. Wang, et al., Efficient methane electrosynthesis enabled by tuning local CO_2 availability, J. Am. Chem. Soc. 142 (7) (2020) 3525–3531.
[15] A. Sedighian Rasouli, et al., CO_2 electroreduction to methane at production rates exceeding 100 mA/cm², ACS Sustain. Chem. Eng. 8 (39) (2020) 14668–14673.
[16] C.A. Obasanjo, et al., High-rate and selective conversion of CO_2 from aqueous solutions to hydrocarbons, Nat. Commun. 14 (1) (2023) 3176.
[17] Y. Xu, et al., Low coordination number copper catalysts for electrochemical CO_2 methanation in a membrane electrode assembly, Nat. Commun. 12 (1) (2021) 2932.
[18] R. Reske, et al., Particle size effects in the catalytic electroreduction of CO_2 on Cu nanoparticles, J. Am. Chem. Soc. 136 (19) (2014) 6978–6986.
[19] Y. Cai, et al., Insights on Forming N,O-Coordinated Cu single-atom catalysts for electrochemical reduction CO_2 to methane, Nat. Commun. 12 (1) (2021) 586.
[20] L. Han, et al., Stable and efficient single-atom Zn catalyst for CO_2 reduction to CH_4, J. Am. Chem. Soc. 142 (29) (2020) 12563–12567.
[21] Q. Zhao, et al., Organic frameworks confined Cu single atoms and nanoclusters for tandem electrocatalytic CO_2 reduction to methane, SmartMat 3 (1) (2022) 183–193.
[22] X. Zhou, et al., Stabilizing Cu^{2+} ions by solid solutions to promote CO_2 electroreduction to methane, J. Am. Chem. Soc. 144 (5) (2022) 2079–2084.
[23] A.J. Welch, et al., Comparative technoeconomic analysis of renewable generation of methane using sunlight, water, and carbon dioxide, ACS Energy Lett. 6 (4) (2021) 1540–1549.
[24] Z.-Z. Niu, et al., Rigorous assessment of CO_2 electroreduction products in a flow cell, Energy Environ. Sci. 14 (8) (2021) 4169–4176.
[25] J.-J. Lv, et al., A highly porous copper electrocatalyst for carbon dioxide reduction, Adv. Mater. 30 (49) (2018) 1803111.
[26] K. Yang, et al., Role of the carbon-based gas diffusion layer on flooding in a gas diffusion electrode cell for electrochemical CO_2 reduction. ACS Energy Lett. 6 (1) (2021) 33–40.
[27] C.M. Gabardo, et al., Combined high alkalinity and pressurization enable efficient CO_2 electroreduction to CO, Energy Environ. Sci. 11 (9) (2018) 2531–2539.
[28] S. Ma, et al., One-step electrosynthesis of ethylene and ethanol from CO_2 in an alkaline electrolyzer, J. Power Sources 301 (2016) 219–228.
[29] S. Ma, et al., Silver supported on titania as an active catalyst for electrochemical carbon dioxide reduction, ChemSusChem 7 (3) (2014) 866–874.
[30] S. Ma, et al., Carbon nanotube containing Ag catalyst layers for efficient and selective reduction of carbon dioxide, J. Mater. Chem. A 4 (22) (2016) 8573–8578.
[31] C.-T. Dinh, et al., CO_2 electroreduction to ethylene via hydroxide-mediated copper catalysis at an abrupt interface, Science 360 (6390) (2018) 783–787.
[32] T. Li, et al., Cu3PdxN nanocrystals for efficient CO_2 electrochemical reduction to methane, Electrochim. Acta 371 (2021) 137793.
[33] H. Zhang, et al., Computational and experimental demonstrations of one-pot tandem catalysis for electrochemical carbon dioxide reduction to methane, Nat. Commun. 10 (1) (2019) 3340.
[34] Y. Liu, et al., Tandem electrocatalytic CO_2 reduction with efficient intermediate conversion over pyramid-textured Cu–Ag catalysts. ACS Appl. Mater. Interfaces 13 (34) (2021) 40513–40521.
[35] K. Zhang, et al., Molecular modulation of sequestered copper sites for efficient electroreduction of carbon dioxide to methane, Adv. Funct. Mater. 33 (17) (2023) 2214062.
[36] C.-J. Chang, et al., Dynamic reoxidation/reduction-driven atomic interdiffusion for highly selective CO_2 reduction toward methane, J. Am. Chem. Soc. 142 (28) (2020) 12119–12132.
[37] G. Zhang, et al., Efficient CO_2 electroreduction on facet-selective copper films with high conversion rate, Nat. Commun. 12 (1) (2021) 5745.
[38] D. Cheng, et al., The nature of active sites for carbon dioxide electroreduction over oxide-derived copper catalysts, Nat. Commun. 12 (1) (2021) 395.
[39] Y. Hori, et al., Electrochemical reduction of carbon dioxide at various series of copper single crystal electrodes, J. Mol. Catal. A Chem. 199 (1) (2003) 39–47.
[40] K.J.P. Schouten, E. Pérez Gallent, M.T.M. Koper, Structure sensitivity of the electrochemical reduction of carbon monoxide on copper single crystals, ACS Catal. 3 (6) (2013) 1292–1295.
[41] K.J.P. Schouten, et al., Two pathways for the formation of ethylene in CO reduction on single-crystal copper electrodes, J. Am. Chem. Soc. 134 (24) (2012) 9864–9867.
[42] F.S. Roberts, K.P. Kuhl, A. Nilsson, High selectivity for ethylene from carbon dioxide reduction over copper nanocube electrocatalysts, Angew. Chem. Int. Ed. 54 (17) (2015) 5179–5182.
[43] F. Chang, et al., Copper-based catalysts for electrochemical carbon dioxide reduction to multicarbon products, Electrochem. Energy Rev. 5 (3) (2022) 4.
[44] P. Iyengar, et al., Size dependent selectivity of Cu nano-octahedra catalysts for the electrochemical reduction of CO_2 to CH_4, Chem. Commun. 55 (60) (2019) 8796–8799.
[45] X.-D. Zhang, et al., Asymmetric low-frequency pulsed strategy enables ultralong CO_2 reduction stability and controllable product selectivity. J. Am. Chem. Soc. 145 (4) (2023) 2195–2206.
[46] Wulff, G., Xxv. Zur Frage Der Geschwindigkeit Des Wachsthums Und Der Auflösung Der Krystallflächen. Zeitschrift für Kristallographie - Crystalline Materials, 1901. 34(1-6): p. 449-530.
[47] A. Hjorth Larsen, et al., The atomic simulation environment-a python library for working with atoms, J. Phys. Condens Matter 29 (27) (2017) 273002.
[48] T.D. Kühne, et al., Cp2k: an electronic structure and molecular dynamics software package - quickstep: efficient and accurate electronic structure calculations, J. Chem. Phys. 152 (19) (2020) 194103.
[49] M. Verstraete, X. Gonze, Smearing scheme for finite-temperature electronic-structure calculations, Phys. Rev. B 65 (3) (2001) 035111.
[50] J. Dennis, On the convergence of Broyden's method for nonlinear systems of equations, Math. Comput. Math. Comput. 25 (1971), p. 559-559.
[51] S. Grimme, et al., A consistent and accurate ab initio parametrization of density functional dispersion correction (DFT-D) for the 94 elements H-Pu, J. Chem. Phys. 132 (15) (2010) 154104.
[52] H. Al-Mahayni, et al., Experimental methods in chemical engineering: density functional theory, Can. J. Chem. Eng. 99 (9) (2021) 1885–1911.
[53] G. Kresse, J. Furthmüller, Efficient iterative schemes for Ab initio total-energy calculations using a plane-wave basis Set, Phys. Rev. B 54 (16) (1996) 11169–11186.
[54] G. Kresse, J. Furthmüller, Efficiency of Ab-Initio total energy calculations for metals and semiconductors using a plane-wave basis Set, Comput. Mater. Sci. 6 (1) (1996) 15–50.
[55] G. Sun, et al., Performance of the vienna ab initio simulation package (Vasp) in chemical applications, J. Mol. Struct. Theochem 624 (1) (2003) 37–45.
[56] G. Kresse, D. Joubert, From ultrasoft pseudopotentials to the projector augmented-wave method, Phys. Rev. B 59 (3) (1999) 1758–1775.
[57] N.A.W. Holzwarth, et al., Comparison of the projector augmented-wave, pseudopotential, and linearized augmented-plane-wave formalisms for density-functional calculations of solids, Phys. Rev. B 55 (4) (1997) 2005–2017.
[58] N. Pueyo Bellafont, et al., Predicting core level binding energies shifts: suitability of the projector augmented wave approach as implemented in Vasp, J. Comput. Chem. 38 (8) (2017) 518–522.
[59] J. Paier, et al., The Perdew–Burke–Ernzerhof exchange-correlation functional applied to the g2-1 test set using a plane-wave basis set, J. Chem. Phys. 122 (23) (2005).
[60] K. Jiang, et al., Metal Ion cycling of Cu foil for selective C–C coupling in electrochemical CO_2 reduction, Nat. Catal. 1 (2) (2018) 111–119.
[61] Y. Wang, J. Liu, G. Zheng, Designing copper-based catalysts for efficient carbon dioxide electroreduction, Adv. Mater. 33 (46) (2021) 2005798.
[62] W. Luo, et al., Facet dependence of CO_2 reduction paths on Cu electrodes, ACS Catal. 6 (1) (2016) 219–229.
[63] W.J. Durand, et al., Structure Effects on the Energetics of the Electrochemical Reduction of CO_2 by copper surfaces, Surf. Sci. 605 (15) (2011) 1354–1359.

[64] Z. Wei, P. Sautet, Improving the accuracy of modelling CO_2 electroreduction on copper using many-body perturbation theory, Angew. Chem. Int. Ed. 61 (43) (2022) e202210060.

[65] G.D. Barmparis, et al., Nanoparticle shapes by using wulff constructions and first-principles calculations, Beilstein J. Nanotechnol. 6 (2015) 361–368.

[66] D. Holec, et al., Surface energy of Au nanoparticles depending on their size and shape, Nanomater. (Basel) 10 (3) (2020).

[67] M.C. Biesinger, Advanced analysis of copper X-ray photoelectron spectra, Surf. Interface Anal. 49 (13) (2017) 1325–1334.

[68] H. Dong, Y. Li, D.-e Jiang, First-principles insight into electrocatalytic reduction of CO_2 to CH_4 on a copper nanoparticle. J. Phys. Chem. C. 122 (21) (2018) 11392–11398.

[69] Q. Zhao, E.A. Carter, Revisiting competing paths in electrochemical CO_2 reduction on copper via embedded correlated wavefunction theory, J. Chem. Theory Comput. 16 (10) (2020) 6528–6538.

[70] Q. Zhao, J.M.P. Martirez, E.A. Carter, Revisiting understanding of electrochemical CO_2 reduction on Cu(111): competing proton-coupled electron transfer reaction mechanisms revealed by embedded correlated wavefunction theory, J. Am. Chem. Soc. 143 (16) (2021) 6152–6164.

[71] J. Hussain, H. Jónsson, E. Skúlason, Calculations of product selectivity in electrochemical CO_2 reduction, ACS Catal. 8 (6) (2018) 5240–5249.

[72] X. Nie, et al., Reaction mechanisms of CO_2 electrochemical reduction on Cu(111) determined with density functional theory, J. Catal. 312 (2014) 108–122.

[73] X. Nie, et al., Selectivity of CO_2 reduction on copper electrodes: the role of the kinetics of elementary steps, Angew. Chem. Int. Ed. 52 (9) (2013) 2459–2462.

[74] R.B. Sandberg, et al., CO-CO coupling on Cu facets: coverage, strain and field effects, Surf. Sci. 654 (2016) 56–62.

[75] J.H. Montoya, A.A. Peterson, J.K. Nørskov, Insights into C-C Coupling in CO_2 electroreduction on copper electrodes, ChemCatChem 5 (3) (2013) 737–742.

[76] J. Santatiwongchai, K. Faungnawakij, P. Hirunsit, Comprehensive mechanism of CO_2 electroreduction toward ethylene and ethanol: the solvent effect from explicit water–Cu(100) interface models, ACS Catal. 11 (15) (2021) 9688–9701.

[77] L.R.L. Ting, et al., Enhancing CO_2 electroreduction to ethanol on copper–silver composites by opening an alternative catalytic pathway. ACS Catal. 10 (7) (2020) 4059–4069.

[78] N. Heidary, K.H. Ly, N. Kornienko, Probing CO_2 conversion chemistry on nanostructured surfaces with operando vibrational spectroscopy, Nano Lett. 19 (8) (2019) 4817–4826.

[79] Z.-Z. Niu, et al., Hierarchical copper with inherent hydrophobicity mitigates electrode flooding for high-rate CO_2 electroreduction to multicarbon products, J. Am. Chem. Soc. 143 (21) (2021) 8011–8021.

[80] J.E. Huang, et al., CO_2 electrolysis to multicarbon products in strong acid, Science 372 (6546) (2021) 1074–1078.

[81] Y. Zhao, et al., Conversion of CO_2 to multicarbon products in strong acid by controlling the catalyst microenvironment, Nat. Synth. (2023).

[82] D. Bhalothia, et al., Reaction pathways for the highly selective and durable electrochemical CO_2 to CO conversion on Zno supported Ag nanoparticles in KCl electrolyte, Appl. Surf. Sci. 608 (2023) 155224.

[83] M. Zhao, et al., Inhibiting hydrogen evolution using a chloride adlayer for efficient electrochemical CO_2 reduction on Zn electrodes, ACS Appl. Mater. Interfaces 12 (4) (2020) 4565–4571.

[84] Z. Ma, et al., CO_2 electroreduction to multicarbon products in strongly acidic electrolyte via synergistically modulating the local microenvironment, Nat. Commun. 13 (1) (2022) 7596.

[85] J. Li, N. Kornienko, Electrocatalytic carbon dioxide reduction in acid, Chem. Catal. 2 (1) (2022) 29–38.

[86] S. Nitopi, et al., Progress and perspectives of electrochemical CO_2 reduction on copper in aqueous electrolyte, Chem. Rev. 119 (12) (2019) 7610–7672.

[87] W. Lai, et al., Stability issues in electrochemical CO_2 reduction: recent advances in fundamental understanding and design strategies, Adv. Mater. 35 (51) (2023) 2306288.

[88] W. Ma, et al., Electrocatalytic reduction of CO_2 to ethylene and ethanol through hydrogen-assisted C–C coupling over fluorine-modified copper, Nat. Catal. 3 (6) (2020) 478–487.